Corrosion-Resistant MoO₃/Fe₂O₃/MoS₂ Heterojunctions Stabilize OH⁻ Adsorption for Efficient Light-Assisted Seawater Electrooxidation

Zhen Li, Wei Tao, Ying Wang, Xucun Ye, Yiqun Chen, Byungchan Han,* and Lawrence Yoon Suk Lee*



Downloaded via HONG KONG POLYTECHNIC UNIV on September 1, 2025 at 08:33:03 (UTC). See https://pubs.acs.org/sharingguidelines for options on how to legitimately share published articles

Cite This: J. Am. Chem. Soc. 2025, 147, 24461-24472



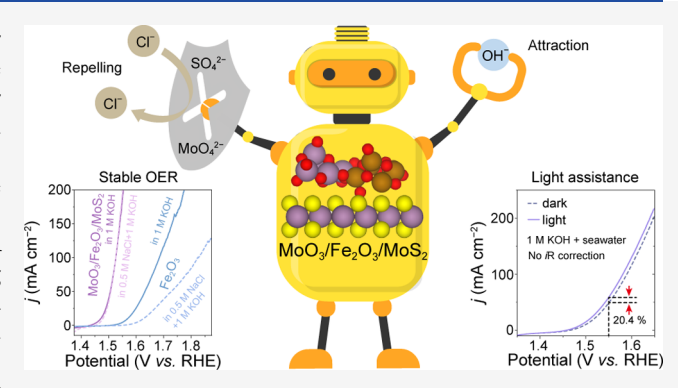
ACCESS I

III Metrics & More

Article Recommendations

Supporting Information

ABSTRACT: Direct seawater electrolysis holds promise for sustainable hydrogen production, yet challenges such as severe chlorine corrosion on the anode and high energy barriers for oxygen evolution reaction (OER) limit its operational time and efficiency. Herein, we present MoO₃/Fe₂O₃/MoS₂ heterojunctions to mitigate chlorine-induced corrosion and achieve effective photoelectric synergy. The in situ leached MoO₄²⁻ and SO₄²⁻ inhibitors reduce Cl⁻ adsorption, thereby ensuring high OER selectivity, while the MoO₃/Fe₂O₃/MoS₂ balances the repelling effects of these inhibitors, facilitating OH- adsorption and widening the overpotential gap between water oxidation and chlorine oxidation. The MoO₃/Fe₂O₃/MoS₂ catalyst outperforms its Fe₂O₃ counterpart in terms of lifespan, maintaining stability at



100 and 300 mA cm⁻² for 100 and 500 h, respectively. Additionally, built-in electric fields formed at the interfaces lower interfacial resistance and extend the lifetime of photogenerated carriers by 1.47-fold, allowing for a 20.4% increase in seawater OER current density under light irradiation. Our findings offer a viable strategy for designing high-performance electrocatalysts for light-assisted seawater electrolysis.

INTRODUCTION

Green hydrogen produced through water electrolysis is pivotal for replacing fossil fuels and achieving carbon neutrality.^{1,2} However, scaling up water electrolysis raises concerns about freshwater shortage.3-6 As a result, seawater electrolysis has gained significant attention as a viable alternative, with seawater constituting 96.5% of the global water supply. Unlike indirect seawater electrolysis, which requires desalination pretreatment, direct seawater electrolysis simplifies the process, offering greater scalability and economic advantages. O,8 Nevertheless, direct seawater electrolysis faces challenges, particularly due to severe corrosion caused by the competitive chlorine evolution reaction (CER) and the high thermodynamic barrier of the oxygen evolution reaction (OER).^{9,10}

Chloride anions in seawater (approximately 0.5 M) can be readily adsorbed on anodes and oxidized to Cl2 or ClO in acidic or alkaline seawaters, respectively, leading to severe corrosion of catalysts and compromised stability. 11,12 For example, Fe₂O₃, a typical OER electrocatalyst, is prone to chlorine-induced corrosion, which limits its applicability in seawater electrolysis. 13 Although alkalizing seawater provides a thermodynamic advantage for OER (Eanode $^{\circ}$ = 1.23 V_{RHE}) over CER ($E_{\text{anode}}^{\circ} = 1.72 \text{ V}_{\text{RHE}}$), Cl⁻ ions can still attack electron-deficient metal sites, fostering competition between

CER and the desired OER, particularly at high current densities. 14,15 Recently, local environmental engineering has been proposed to enhance OER selectivity. 16 Anion species such as SO_4^{2-} and MoO_4^{2-} introduced during the electrocatalytic process has been shown to form permselective protective layers that repel Cl through electrostatic repulsion. 17-21 However, these anion-enriched regions may also impede the diffusion of OH⁻ ions, potentially obstructing OER.²² Addressing the challenge of alleviating the repelling effect of anion inhibitors on OH- to ensure robust OER activity in seawater remains a significant task. Recent studies have demonstrated that constructing heterojunctions can create robust catalytic interfaces that modulate the electronic structure and OH⁻ adsorption behavior, thereby lowering the reaction energy barrier and improving electrocatalytic OER performance.^{23–25} For instance, heterojunctions composed of

Received: March 8, 2025 Revised: May 23, 2025 Accepted: May 27, 2025 Published: June 3, 2025





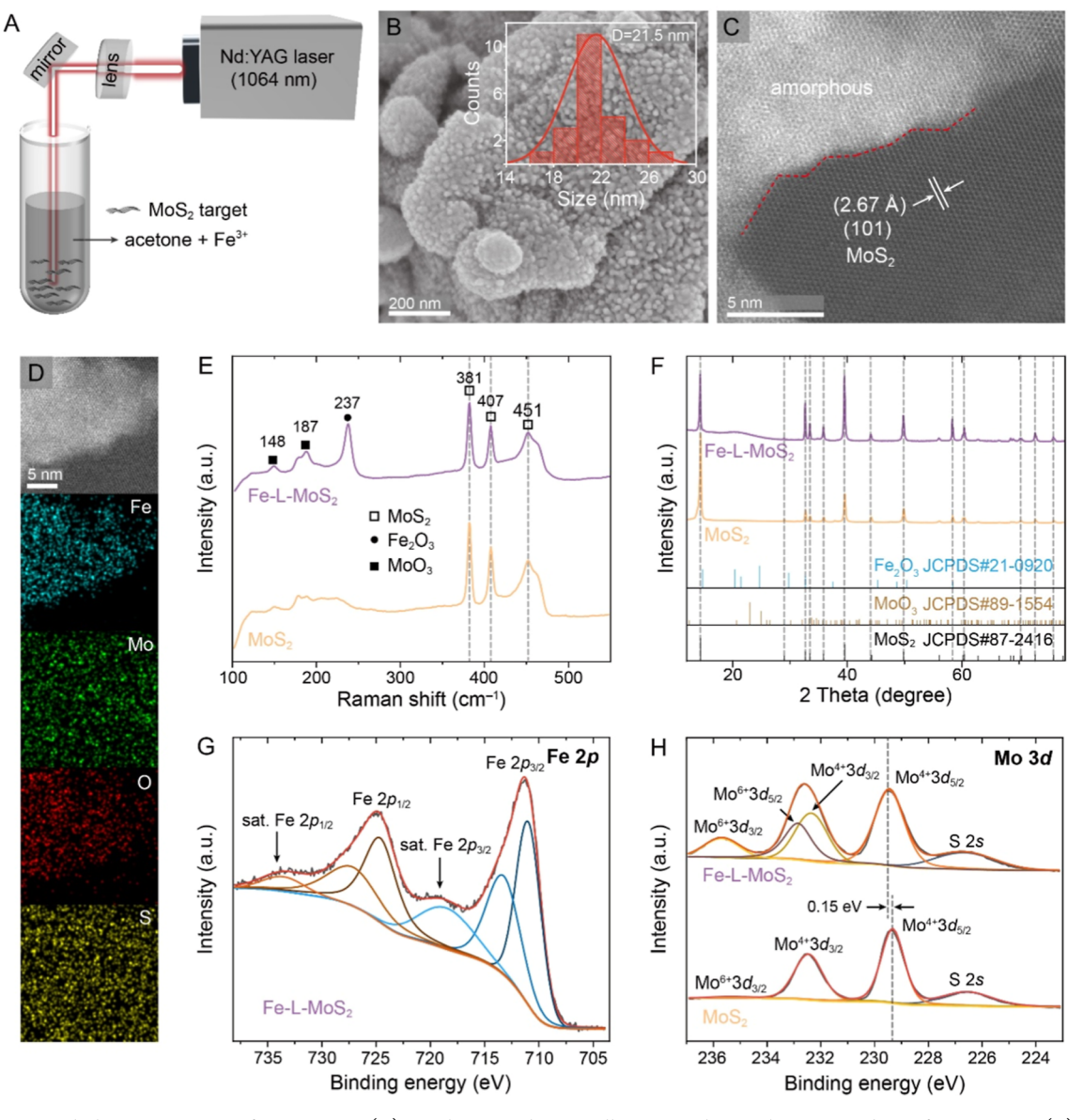


Figure 1. Structural characterizations of Fe-L-MoS₂. (A) A schematic diagram illustrating the synthetic procedure of Fe-L-MoS₂. (B) SEM (C) high-resolution TEM, and (D) STEM images with the corresponding EDS mapping images of Fe-L-MoS₂. (E) Raman spectra and (F) XRD patterns of MoS₂ and Fe-L-MoS₂. XPS (G) Fe 2p spectrum of Fe-L-MoS₂ and (H) Mo 3d spectra of MoS₂ and Fe-L-MoS₂.

Fe- and Mo-based materials, such as Fe_2O_3/MoO_3 and $Fe_2O_3/P-CoMoO_4$, exhibit superior OER activity compared to their single-component counterparts. This enhancement is primarily attributed to the strongly coupled interfaces that facilitate charge redistribution and optimize reactant adsorption energy.

Inspired by electro-assisted photocatalysis strategies, photogenerated carrier-assisted electrocatalysis has recently emerged as a promising approach to improve water-splitting performance. This innovative strategy utilizes light energy to excite a photoactive component, generating carriers that promote the electrochemical reaction on the electro-active component by lowering overpotentials or increasing catalytic current densities. 30,31 Light assistance serves as an excellent supplement for water electrolysis due to its effective utilization of clean solar energy and ease of application. While most studies on light-assisted water electrolysis have focused on broadening the absorption spectrum or modifying the electro-active component, $^{32-35}$ the transfer of photogenerated carriers

between photoactive and electro-active components in light-assisted electrocatalytic OER systems has been largely overlooked. Inefficient carrier transfer often results in rapid recombination of photogenerated electrons and holes, limiting their utilization in catalytic reactions.^{36–38} Previous reports demonstrated that introducing a built-in electric field through heterojunction formation could effectively facilitate the migration of photogenerated carriers to active sites, enabling their participation in catalytic reactions.^{39–42} For light-assisted seawater electrolysis, the primary challenge lies in simultaneously mitigating chlorine corrosion and achieving efficient photoelectric coupling.

In this study, we present an efficient and stable seawater oxidation electrocatalyst, $MoO_3/Fe_2O_3/MoS_2$, which exhibits exceptional OER selectivity and photoelectric coupling effect. Nanosized particles and amorphous—crystalline interfaces, induced by laser ablation, effectively increase the electrochemical surface area, enabling efficient mass diffusion. MoO_4^{2-} and SO_4^{2-} ions, leached during the OER activation

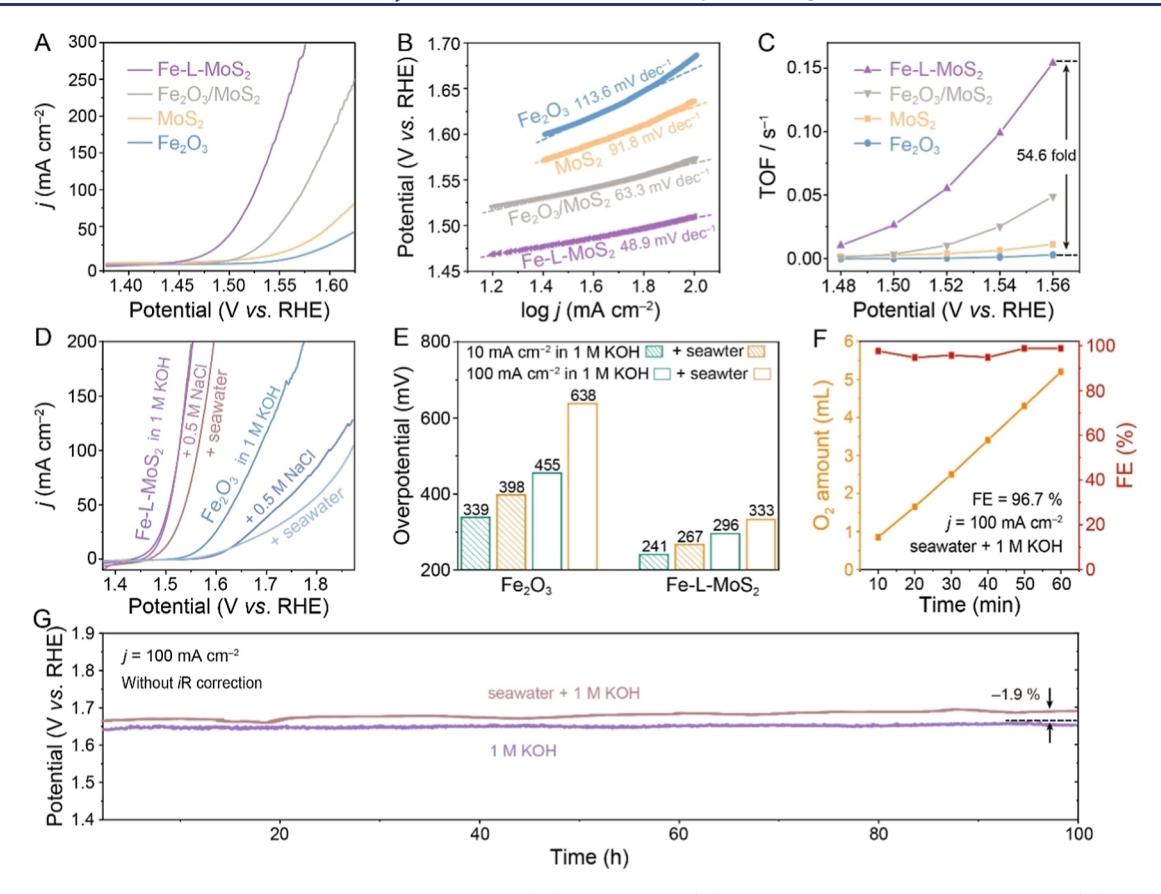


Figure 2. OER performance in alkaline freshwater and seawater. (A) LSV curves, (B) the corresponding Tafel slopes, and (C) TOF of Fe_2O_3 , MoS_2 , Fe_2O_3/MoS_2 , and Fe_2L-MoS_2 . (D) LSV curves of Fe_2L-MoS_2 and Fe_2O_3 in alkaline saline water and seawater. (E) Comparison of OER overpotentials of Fe_2L-MoS_2 and Fe_2O_3 in various electrolytes. (F) FE (red squares) of Fe_2L-MoS_2 measured at 100 mA cm⁻² in alkaline seawater. Yellow squares indicate the amount of O_2 generated during the FE test. (G) Chronopotentiograms of Fe_2L-MoS_2 in alkaline freshwater and seawater.

process, contribute to repelling Cl ions in seawater. Additionally, the MoO₃/Fe₂O₃/MoS₂ heterojunctions are particularly advantageous for ensuring OH⁻ adsorption and widening the potential gap between OER and CER, thus mitigating catalyst corrosion. Furthermore, the dual built-in electric fields formed at the three-phase heterointerfaces facilitate the rapid migration of photogenerated carriers and reduce interfacial resistance, allowing more charges to participate in OER. As a result, the ternary hybrid catalyst demonstrates remarkable OER performance, achieving a current density of 10 mA cm⁻² at a low overpotential of 267 mV in alkaline seawater and maintaining excellent stability at 100 and 300 mA cm⁻² for 100 and 500 h, respectively. Moreover, light irradiation enhances the current density for seawater oxidation by 20.4%. The MoO₃/Fe₂O₃/MoS₂||Pt/C electrolyzer operates stably at an industry-required current density of 1 A cm⁻² in alkaline seawater with light assistance for over 50 h. This work presents a promising strategy for developing light-assisted seawater electrolysis, paving the way for sustainable green hydrogen production.

■ RESULTS AND DISCUSSION

Synthesis and Characterizations of Fe-L-MoS₂. Bulk MoS₂ powder was ablated with a pulsed laser in acetone containing Fe(NO₃)₃ (0.05 M) for 25 min to produce MoS₂ microparticles (denoted as Fe-L-MoS₂) decorated with numerous nanoparticles (D = 21.5 nm, Figure 1A,B). During the laser ablation process, the MoS₂ powder transforms into a

mixture of microparticles and microplates (Figure S2a-d). The duration of laser ablation significantly influences the morphology, with microparticles gradually dominating as the ablation time is extended (Figure S2b-g). The Brunauer-Emmett-Teller (BET) adsorption-desorption isotherms and specific surface areas of samples are present in Figure S3 and Table S1, respectively. The BET surface area of Fe-L-MoS₂ $(47.35 \text{ m}^2 \text{ g}^{-1})$ is 5.7 times greater than that of pristine MoS₂ $(8.33 \text{ m}^2 \text{ g}^{-1})$, providing more active sites for catalytic reaction. High-resolution transmission electron microscopic (TEM) image of Fe-L-MoS₂ (Figure 1C) reveals lattice fringes with an interplanar spacing of 2.67 Å, corresponding to the (101) plane of MoS2, and a distinct boundary (red dashed line) separating crystalline and amorphous regions. The amorphous regions suggest defect-rich structures, indicative of MoO3 and Fe₂O₃ formation. Scanning TEM (STEM) and the corresponding energy-dispersive X-ray spectroscopy (EDS) mapping images (Figure 1D) show uniform distributions of Mo and S across Fe-L-MoS2, with Fe and O enriched in the amorphous regions, supporting the presence of Fe₂O₃ and MoO₃. The content of Mo and Fe elements before and after laser ablation was quantified using inductively coupled plasma optical emission spectroscopy (ICP-OES) and is summarized in Table S2. The Fe/Mo ratio increases with extended laserablation time, exceeding 1.0 for ablation durations longer than 25 min, indicating successful incorporation of Fe as a secondary component, rather than merely as a dopant.

The Raman peak observed at 237 cm⁻¹ in Fe-L-MoS₂ is attributed to the A_{1g} symmetric stretching vibrations of the Fe-O band (Figure 1E), aligning with the Raman spectrum of Fe₂O₃/MoS₂ (Figure S4b), which suggests the formation of Fe₂O₃ after laser ablation. ⁴³ In addition to the characteristic Raman peaks of MoS₂ at 381, 407, and 451 cm⁻¹, ⁴⁴ two new peaks attributed to MoO₃ are observed at 148 and 187 cm^{-1,45} These observations indicate the coexistence of MoO₃ and Fe₂O₃ within Fe-L-MoS₂. However, the X-ray diffraction (XRD) pattern of Fe-L-MoS₂ (Figure 1F) is predominantly characterized by MoS2 peaks, with a broad peak at approximately 21° indicating the presence of amorphous Fe₂O₃ and MoO₃ phases. The prominent peak at 14.5°, corresponding to the (002) plane of MoS₂, indicates a strong preferential orientation of the MoS₂ layers, the intrinsic interlayer stacking of MoS₂ sheets. A possible formation mechanism involves a transient plasma plume, characterized by high temperature and high pressure, generated on the MoS₂ target surface during pulsed laser irradiation. This plume contains oxygen and hydroxyl radicals, 46,47 which rapidly oxidize a portion of MoS₂ to MoO₃ in water (Figure S5). To mitigate excessive MoS2 oxidation, acetone was employed as the solvent for laser ablation, as it generates reducing gases (e.g., CH₄ and CO) that inhibit oxidation. 48 Concurrently, tions adsorbed on negatively charged MoS2 (Figure S6) can easily transform into amorphous species due to the rapid cooling property of laser ablation. Figure 1G shows the X-ray photoelectron spectrum (XPS) of Fe-L-MoS₂ in the Fe 2p region. Two distinct peaks at binding energies of 711.1 (Fe $2p_{3/2}$) and 724.4 eV (Fe $2p_{1/2}$) are observed, along with satellite peaks at 719.1 and 733.8 eV, consistent with reported Fe₂O₃ results. 49 Additionally, the peak at 713.5 eV is attributed to the Fe³⁺-SO₄²⁻ bond. Unlike pristine MoS₂, two peaks at 531.0 and 530.1 eV, which can be assigned to Mo-O and Fe-O bonds, respectively, dominate in the O 1s spectrum of Fe-L-MoS₂ (Figure S7b), further confirming the formation of MoO₃ and Fe₂O₃. 51,52 Similarly, in the Mo 3d spectrum of Fe-L- MoS_2 , two new peaks for Mo^{6+} $3d_{5/2}$ and Mo^{6+} $3d_{3/2}$ are observed at 232.9 and 235.7 eV, respectively (Figure 1H). Notably, the Mo⁴⁺ peak at 229.35 eV shifts by 0.15 eV toward higher binding energy, indicative of reduced electronic density around Mo atoms and suggesting strong interaction among the three components.⁵³ The Mo⁶⁺/Mo⁴⁺ atomic ratios of Fe-L-MoS₂ samples synthesized using different laser ablation times are estimated (Figure S8) and summarized in Table S3. This ratio increases with the laser ablation time, reaching a value of 0.48 at 25 min-ablation. Furthermore, the S-Fe bond is identified at 162.7 eV in the S 2p spectrum (Figure S7c), 54,55 consistent with the Fe 2p results and indicating the interaction between Fe₂O₃ and MoS₂.

Electrocatalytic Performance in Alkaline Freshwater and Seawater. The OER activity of the as-prepared samples was evaluated in O₂-saturated 1 M KOH using a standard three-electrode cell. Figure 2A compares linear sweep voltammograms (LSVs) collected at a scan rate of 2 mV s⁻¹. Fe-L-MoS₂ requires overpotentials of 241 and 296 mV to reach current densities of 10 and 100 mA cm⁻², respectively (Figure S9a), which are significantly lower compared to Fe₂O₃/MoS₂ (282 and 343 mV), pristine MoS₂ (307 and 406 mV), and Fe₂O₃ (339 and 455 mV). The Tafel plots derived from the polarization curves reveal that Fe-L-MoS₂ exhibits the lowest Tafel slope (48.9 mV dec⁻¹) among all samples investigated (Figure 2B), indicating its rapid reaction kinetics. When

comparing OER overpotential at 10 mA cm⁻² and Tafel slope, Fe-L-MoS₂ outperforms or matches other benchmark MoS₂and Fe₂O₃-based catalysts (Figure S9b and Table S4). Moreover, Fe-L-MoS₂ demonstrates a high turnover frequency (TOF) value of 0.154 s⁻¹ (Figure 2C), approximately 54.6 times that of Fe₂O₃ (0.003 s⁻¹), highlighting the substantial enhancement of intrinsic catalytic activity achieved through the formation of amorphous/crystalline heterojunctions. The OER performance of Fe-L-MoS₂ can be optimized by adjusting the Fe³⁺ concentration and laser-ablation time (Figure S10). The lowest OER overpotential is achieved with a sample synthesized using 0.05 M Fe(NO₃)₃ and 25 min of ablation, yielding a 34.2% Fe₂O₃ content and a Mo⁶⁺/Mo⁴⁺ ratio of ca. 0.48 (Figure S11). Acetone's low polarity enhances Fe₂O₃ deposition on the sample surface, thereby improving its OER activity (Figure S12). Excessive laser ablation or Fe³⁺ usage decreases OER performance due to increased charge transfer resistance (Figure S13), likely caused by the excessive formation of Fe₂O₃ and MoO₃ (Table S3).

The OER activity of Fe-L-MoS₂ was further evaluated in alkaline saline (0.5 M NaCl + 1 M KOH) and alkaline natural seawater (seawater +1 M KOH) electrolytes to explore its potential for seawater electrolysis application. As shown in Figure 2D, Fe-L-MoS₂ exhibits superior OER performance with minimal activity decline in saline water electrolytes, indicating that the impact of highly concentrated Cl⁻ ions on its catalytic activity is not significant. However, a noticeable deterioration in OER performance is observed in the alkaline seawater, which can be attributed to the presence of bacteria, microbes, and insoluble precipitates formed during the seawater OER process.⁵⁶ In alkaline seawater, the Fe-L-MoS₂ electrode requires only 267 and 333 mV to reach 10 and 100 mA cm⁻², respectively (Figure 2E), which are considerably lower than those of Fe_2O_3 (398 and 638 mV) under the same conditions. Notably, the electrode achieves a high average Faradaic efficiency (FE) of 96.7% at a large current density of 100 mA cm⁻² in alkaline seawater (Figure 2F). Iodide titration was engaged to detect the generation of reactive chlorine species.⁵⁷ No characteristic absorption peak of hypochlorite ions is observed in the electrolyte after the FE test (Figure S14b), indicating the catalyst's high selectivity for OER over the hypochlorite formation reaction. Operational stability is another crucial parameter for electrocatalysts. To assess the electrocatalytic durability of Fe-L-MoS2 during OER, longterm chronopotentiometry was conducted in both alkaline freshwater and seawater. Remarkably, Fe-L-MoS₂ demonstrates excellent stability at a current density of 100 mA cm⁻² in both alkaline electrolytes over a 100 h period (Figure 2G), with only a slight increase (1.89%) in the required potential for seawater OER.

Exploration of OER and Anticorrosion Mechanisms. Reconstruction is a common occurrence during the OER activation process. After OER activation, the XRD pattern of Fe-L-MoS₂, excluding the Ni foam substrate, continues to be dominated by the MoS₂ phase (Figure S15a), indicating that no new species are formed during activation. In the Raman spectra (Figure S15b), all peaks corresponding to MoS₂, Fe₂O₃, and MoO₃ remain at the same positions. However, the intensity of the MoS₂ peak is slightly reduced compared to that of Fe₂O₃, suggesting a minor loss of MoS₂. Postactivation, Fe-L-MoS₂ retains its morphology, characterized by microparticles decorated with nanoparticles (Figure S16). High-resolution TEM images (Figure S17a) show an interplanar spacing of 2.7

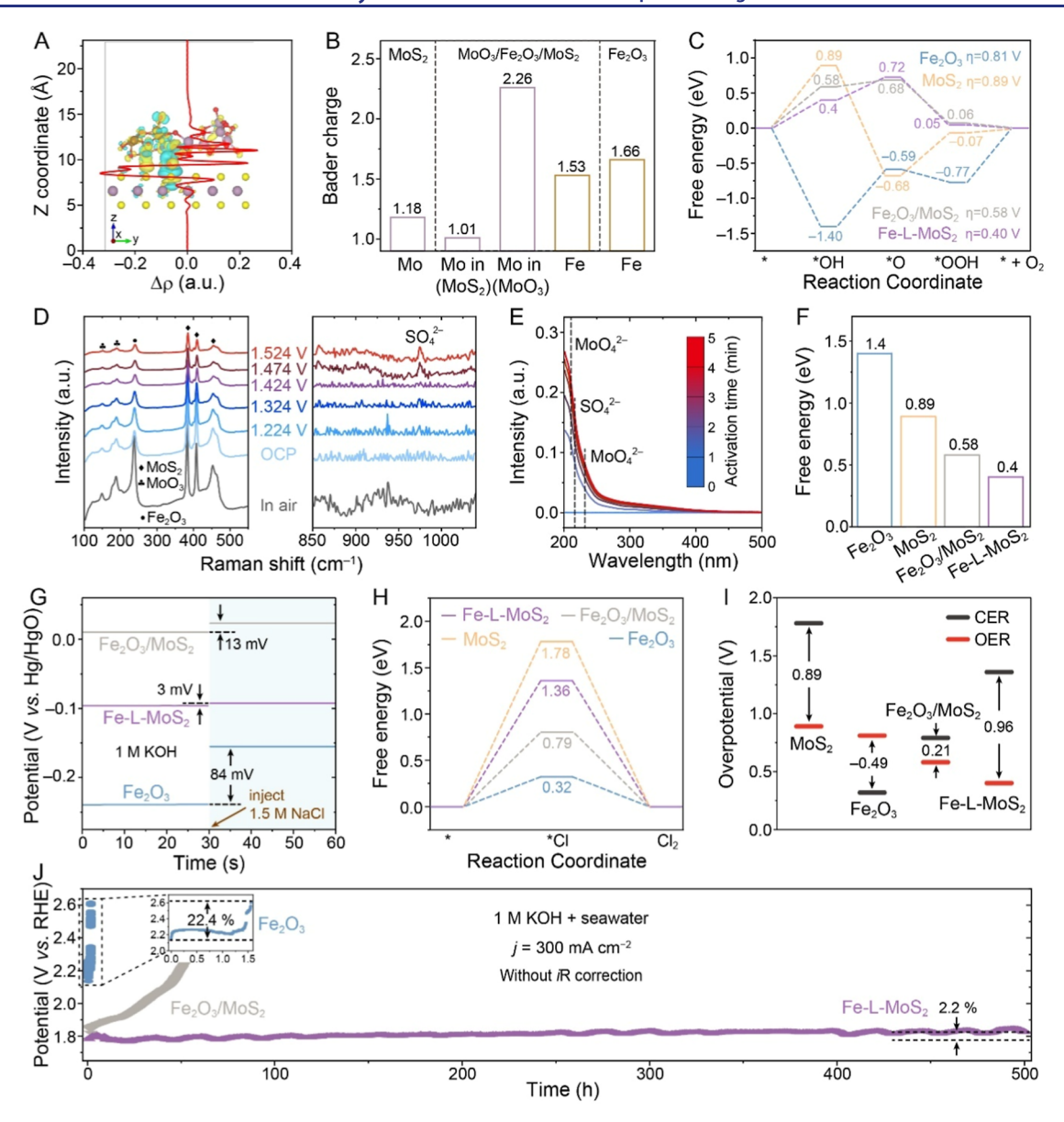


Figure 3. OER and corrosion-resistant mechanisms. (A) Charge density difference and planar average charge density difference (red line) along the z-direction of the MoO₃/Fe₂O₃/MoS₂ heterojunction in Fe-L-MoS₂. (B) Charges on Mo and Fe in Fe₂O₃, MoS₂, and Fe-L-MoS₂. (C) Gibbs free energy diagrams for OER. (D) In situ Raman spectrum of Fe-L-MoS₂. (E) Quasi-in situ UV—vis spectra for MoO₄²⁻ and SO₄²⁻ detection. (F) Free energy change on $E_{*OH} - E_{slab}$, (G) OCP profiles (H) Gibbs free energy diagrams for CER, and (I) the corresponding overpotential gaps between OER and CER for Fe₂O₃, MoS₂, Fe₂O₃/MoS₂, and Fe-L-MoS₂ in seawater +1 M KOH.

Å, corresponding to the (100) plane of MoS_2 , along with several amorphous regions. EDS mapping images (Figure S17b) confirm the uniform distribution of Mo, Fe, O, and S elements across the activated sample. These results collectively indicate that Fe-L-MoS₂ largely maintains its structural integrity after OER activation. Notably, the presence of MoO_4^{2-} and SO_4^{2-} is observed in the XPS spectra (Figure S18) following OER activation, which may play a significant role in enhancing anticorrosion properties.

Density functional theory (DFT) calculations were conducted to gain insights into how heterojunctions enhance both the water oxidation activity and anticorrosion properties of catalysts. Models of amorphous Fe₂O₃, amorphous/crystalline Fe₂O₃/MoS₂, and MoO₃/Fe₂O₃/MoS₂ heterojunctions were constructed using ab initio molecular dynamics simulations, and their crystal structures are provided in Figure S19. The

charge redistribution across the three-phase heterojunction in Fe-L-MoS $_2$ was quantitatively analyzed using planar-averaged differential charge density ($\Delta\rho$). Positive and negative values indicate charge accumulation and depletion, respectively. Figure 3A shows the $\Delta\rho$ profile along the z-direction (perpendicular to the interface), with charge accumulation and depletion depicted in yellow and cyan regions. Along the z-axis, charge depletion is observed at the interface between the MoS $_2$ and the two amorphous oxides, while charge accumulation occurs where the two amorphous oxides are located. This result suggests charge transfer from the MoS $_2$ to the amorphous oxides upon heterointerface formation.

Bader charge distributions at the binary and ternary heterointerfaces are given in Figure S20. The net charge at the Mo site in the MoS_2 phase of the Fe_2O_3/MoS_2 heterointerface is higher than in the pristine MoS_2 phase

(Figure S21), while the charge at the Fe site in the Fe₂O₃ phase is lower than in single-phase Fe₂O₃, indicating charge transfer from MoS₂ to Fe₂O₃. Upon incorporating a third phase, MoO₃, to form the MoO₃/Fe₂O₃/MoS₂ ternary heterointerface, the Mo site in MoO₃ exhibits a higher Bader charge compared to single-phase MoS₂ (Figure 3B), while the Fe site has a lower Bader charge compared to single-phase Fe₂O₃. This confirms charge transfers from MoO₃ to Fe₂O₃ in the ternary heterojunction, suggesting Fe as the reactive site. The change in Bader charge at Fe and Mo sites in MoO₃/Fe₂O₃/MoS₂ compared to the binary hybrid can be ascribed to the strong interaction in the ternary heterointerface.

Electrochemical impedance spectroscopy (EIS) was employed to probe the charge transfer process, and the Nyquist plots are provided in Figure S22 and Table S5. The catalyst resistance (R_2) for MoS $_2$ (0.61 Ω), Fe $_2$ O $_3$ (3.30 Ω), and Fe $_2$ O $_3$ /MoS $_2$ (1.26 Ω) is considerably reduced to 0.24 Ω in Fe-L-MoS $_2$, demonstrating the effective synergistic effects of three-phase heterointerfaces in lowering the charge transfer barrier in electrocatalysts. The solid–liquid interface resistance ($R_{\rm ct}$) also decreases from 114.50 Ω (Fe $_2$ O $_3$) and 74.67 Ω (MoS $_2$) to 2.0 Ω in Fe-L-MoS $_2$, indicating facilitated charge exchange between the electrode and the electrolyte, as well as improved OER kinetics. The formation of heterointerfaces promotes charge redistribution within the space charge layer at the electrode—solution interface.

Mott–Schottky analysis was performed to assess charge concentration by measuring capacitance across a range of applied potentials. ⁵⁹ The Mott–Schottky plot for Fe-L-MoS $_2$ reveals a carrier density of 5.39 \times 10^{21} cm $^{-3}$, which is approximately 14.9, 18.7, and 54.2 times greater than that of the Fe $_2$ O $_3$ /MoS $_2$ hybrid (3.61 \times 10^{20} cm $^{-3}$), pristine MoS $_2$ (2.88 \times 10^{20} cm $^{-3}$), and Fe $_2$ O $_3$ (9.95 \times 10^{19} cm $^{-3}$), respectively (Figure S23). This enhanced carrier density indicates that the Fe-L-MoS $_2$ interface provides more mobile charges available for catalytic reactions, potentially contributing to improved catalytic performance.

DFT calculations were also employed to determine the free energy diagrams for each elementary step during the OER (Figures S24–S27). The OER free energy diagram in Figure 3C reveals that for Fe₂O₃, the rate-determining step (RDS) is the deprotonation and electron transfer from *OH to form *O (the second step). In contrast, for both Fe₂O₃/MoS₂ and Fe-L-MoS₂, the RDS shifts to the *OH adsorption (the first step). At the same time, the overall OER free energy decreases significantly from 0.81, 0.89, and 0.58 eV for Fe₂O₃, MoS₂, and Fe₂O₃/MoS₂, respectively, to 0.40 eV for Fe-L-MoS₂, highlighting the beneficial effects of heterointerfaces on OER catalysis.

To further investigate the impact of interfaces on OER thermodynamics, Arrhenius plots of Fe_2O_3 , MoS_2 , and Fe-L- MoS_2 were obtained by measuring LSVs at various temperatures (Figures S28 and S29). The activation energy (E_a), extracted from the slope of the Arrhenius plot, is the lowest fee-L- MoS_2 (23.5 kJ mol^{-1}), followed by Fe_2O_3/MoS_2 (37.4 kJ mol^{-1}), MoS_2 (41.3 kJ mol^{-1}), and Fe_2O_3 (53.5 kJ mol^{-1}). This reduction in E_a indicates a significant decrease in the kinetic barrier for electrocatalytic water oxidation at the heterojunctions. Electrochemical surface areas (ECSAs) of the as-prepared catalysts were also determined using electrochemical double-layer capacitance (C_{dl}) from cyclic voltammograms (Figures S30 and S31). Notably, Fe-L- MoS_2 exhibits an ECSA of 4.88 cm² mg^{-1} , which is smaller than that of pristine

MoS₂ (6.82 cm² mg⁻¹). This indicates there is no clear positive correlation between specific surface area and specific capacitance. The large and complete layered structure of MoS₂ is more conducive to promoting the reversible insertion and extraction of ions in the electrolyte, thereby exhibiting superior capacitance. After normalizing the polarization curves by ECSA (Figure S32), Fe-L-MoS₂ maintains superior OER activity compared to its counterparts. This suggests that its outstanding performance stems from enhanced intrinsic catalytic activity facilitated by the three-phase interfaces.

In situ Raman spectroscopy was employed to monitor surface species as the applied potential varies in real time. Figure 3D presents the in situ Raman spectra of Fe-L-MoS₂ collected between the open-circuit potential (OCP) and an applied potential of 1.524 V. Characteristic peaks corresponding to MoO₃, Fe₂O₃, and MoS₂ are evident at the OCP, with decreasing intensity as applied potential increases. Notably, a new peak at 975 cm⁻¹, attributed to SO₄²⁻, appears at 1.474 V,60 indicating the oxidation of MoS2 during the OER process. Quasi-in situ UV-vis spectroscopy further confirms the release of MoO₄²⁻ and SO₄²⁻ anions (Figure S33). Upon applying 2.5 V to Fe-L-MoS₂ in a two-electrode system, absorption peaks for MoO₄²⁻ (211 and 232 nm) and SO₄²⁻ (216 nm) appear after 1 min (Figure 3E). These peaks intensify with prolonged oxidation time, substantiating the release of MoO₄²⁻ and SO_4^{2-} from MoS_2 .

The presence of MoO₄²⁻ and SO₄²⁻ anions around Fe-L-MoS₂, formed under anodic potential, can repel Cl⁻ through electrostatic repulsion, thereby mitigating corrosion during seawater oxidation.¹⁹ Additionally, Fe-L-MoS₂ exhibits the smallest energy gap between E_{*OH} and E_{slab} (Figure 3F), indicating that the heterojunction enhances OH- adsorption, counteracting the electrostatic repulsion from anions. The strong hydrogen bonding between OH- and MoS2 further prevents electrostatic repulsion during OH⁻ diffusion, ensuring rapid OER kinetics. 61 This is supported by the OCP measurements, which reflect Cl⁻ adsorption on the Helmholtz layer; a greater influence of the catalyst surface on Cl⁻ results in a more profound shift in OCP upon introducing Cl^{-62,63} Typically, the exchange of adsorbates and ions within the Helmholtz layer disrupts the electrode potential equilibrium. Upon adding 1.5 M NaCl to the electrolyte, a significant increase in OCP of 84 mV is observed for Fe₂O₃ compared to Fe₂O₃/MoS₂ (13 mV, Figure 3G). This change further decreases to 3 mV for Fe-L-MoS2, demonstrating that the coupling effect of MoO₄²⁻/SO₄²⁻ ions and MoO₃/Fe₂O₃/ MoS₂ heterojunctions in Fe-L-MoS₂ can further stabilize the Helmholtz layer. In other words, the heterojunction balances the electrostatic effects of anion inhibitors on OH- and stabilizes OH⁻ adsorption. XPS analysis post-OER activation in saline electrolyte (0.5 M NaCl + 1 M KOH) reveals a Cl 2p peak at 198.3 eV for Fe₂O₃ (Figure S34a), confirming Cl⁻ adsorption,⁶⁴ whereas no Cl⁻ signal is detected for Fe-L-MoS₂ (Figure S34b), underscoring its superior Cl--repelling property. Although the overpotential gap at 100 mA cm⁻² between freshwater and saline water is reduced from 139 mV on Fe₂O₃ to 10 mV on Fe₂O₃/MoS₂ (Figure S35b), the OER performance in saline water remains inferior to that in freshwater due to the repelling effect of leached MoO₄²⁻ and SO₄²⁻ on OH⁻ adsorption. Notably, Fe-L-MoS₂ exhibits similar LSV curves in both electrolytes (Figure S35a). The overpotential gap is further reduced to 0 mV with Fe-L-MoS₂, indicating that the MoO₃/Fe₂O₃/MoS₂ heterojunction effec-

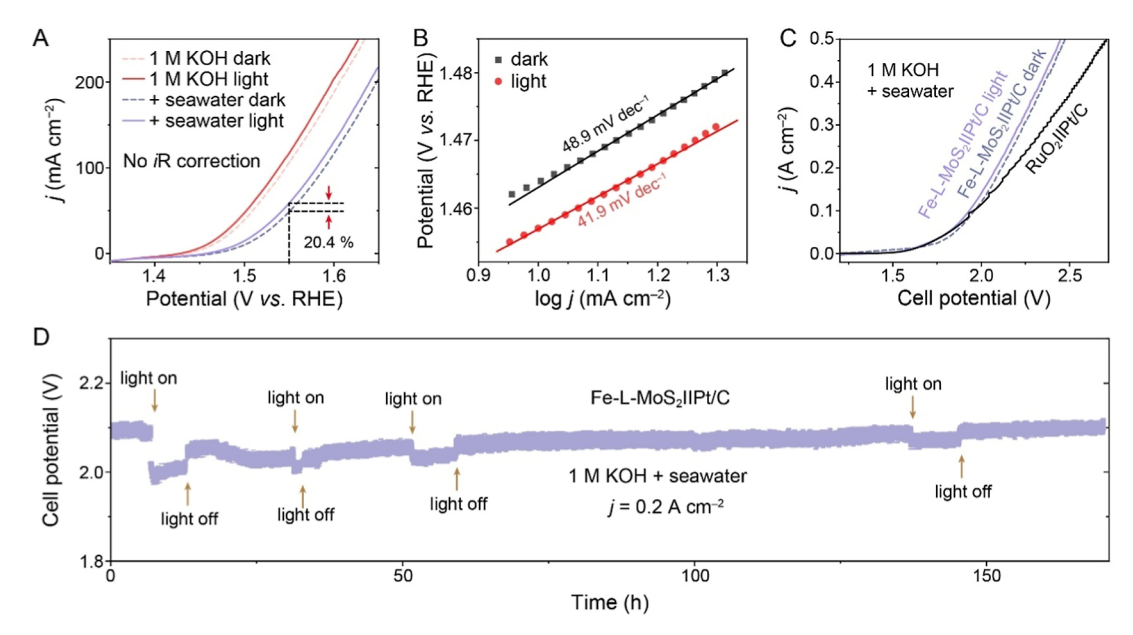


Figure 4. Light-assisted OER and seawater electrolysis performance. (A) LSV curves of Fe-L-MoS₂ in the dark and under light irradiation in various electrolytes and (B) the corresponding Tafel plots. (C) LSV curves measured using two-electrode systems of Fe-L-MoS₂||Pt/C and RuO₂||Pt/C. (D) Chronopotentiogram of Fe-L-MoS₂||Pt/C alkaline seawater electrolyzer operated at 0.2 A cm⁻².

tively balances the repelling influence of anion inhibitors on OH^- , thereby ensuring OH^- adsorption for efficient OER catalysis. Considering that adsorbed Cl^- ions on active sites can hinder the oxidation of OH^- , thereby limiting OER catalysis, the OER activity, particularly at low current densities, is positively correlated with the number of effective active sites. As shown in Figure S36a, Fe_2O_3 exhibits a 16.3% decrease in current density at the onset potential when the electrolyte is switched to 1 M KOH + 0.5 M NaCl. This suggests that 16.3% of the active sites are poisoned by Cl^- ions. In contrast, Fe-L-MoS $_2$ shows no decrease in current density under the same conditions (Figure S36b), indicating its superior Cl^- -repelling properties.

The CER process in Fe-L-MoS₂ was investigated using a two-step Volmer-Heyrovsky mechanism, encompassing Cladsorption and subsequent molecular Cl₂ release (Figures \$37-\$40). The Gibbs free energy changes for each elementary step of the CER are presented in Figure 3H. The free energy diagram indicates that Fe-L-MoS2 requires substantially higher energy (1.36 eV) for CER compared to Fe₂O₃ (0.32 eV), signifying that the heterojunction effectively suppresses CER, thereby enhancing the corrosion resistance of the electrode. MoS₂ exhibits the greatest free energy for CER due to the unfavorable Cl- adsorption on S sites. Additionally, the thermodynamic OER selectivity can be described by the overpotential gap between OER and CER ($\eta_{\rm CER}$ - $\eta_{\rm OER}$), where a large gap indicates a higher selectivity of OER. The overpotential gap for Fe₂O₃ is determined to be -0.49 V (Figure 3I), suggesting that CER is more favorable than OER. In contrast, positive overpotential gap values for MoS₂, Fe₂O₃/ MoS₂, and Fe-L-MoS₂ indicate that OER dominates the anodic reaction, with Fe-L-MoS₂ exhibiting the largest gap of 0.96 V for enhanced OER selectivity.

Long-term seawater electrolysis at a high current density of 300 mA cm^{-2} was conducted on Fe_2O_3 , Fe_2O_3/MoS_2 , and Fe_2O_3 (Figure 3J). Fe-L-MoS₂ maintains relatively stable activity over 500 h, while Fe_2O_3 and Fe_2O_3/MoS_2 rapidly lose activity within 1.5 and 53 h, respectively. Although Fe_2O_3/MoS_2 and Fe_2O_3/MoS_2 rapidly lose

MoS₂ exhibits a slight increase (2.2%) in the potential required to sustain 300 mA cm⁻² for seawater OER, this is significantly less than the 22.4% increase observed for Fe₂O₃ within just 1.5 h, further confirming the excellent corrosion resistance of Fe-L- MoS_2 . The voltage degradation rate (D_U) is calculated using $D_{
m U}=rac{\overline{U_2}-\overline{U_1}}{t}$, where \overline{U}_1 and \overline{U}_2 are the average potentials during the initial and final 10% of the test duration (t), respectively, to mitigate fluctuations in long-term operation. 65 In a 500 h chronopotentiometry test at 300 mA cm⁻², Fe-L-MoS₂ exhibits a D_U of 0.078 mV h⁻¹, significantly lower than that of Fe₂O₃ (0.319 mV h⁻¹), demonstrating its superior stability for seawater electrolysis. Notably, no characteristic absorption peak of hypochlorite ions is observed in the electrolyte after the 500 h catalytic operation (Figure S41), indicating the high selectivity of Fe-L-MoS₂ for the OER over the hypochlorite formation reaction, even at higher current densities. Corrosion polarization curves obtained in natural seawater show that Fe-L-MoS₂ has a significantly lower corrosion current density (0.101 mA cm⁻²) and a higher corrosion potential (-0.28 V) compared to Fe₂O₃ (1.101 mA cm^{-2} and -0.37 V), indicating stronger corrosion resistance in seawater (Figures S42 and S43).⁶⁶ Notably, the Raman peaks for Mo-O, Fe-O, and Mo-S vibrations are observed after OER activation and a 100 h stability test in alkaline seawater (Figure S44), suggesting the integrity of the three-phase structure. However, the intensity of the Mo-S mode has diminished relative to the Fe-O mode after OER activation, likely due to the oxidation of MoS₂. The nanoparticles on Fe-L-MoS₂ are preserved during seawater electrolysis (Figure S45a), confirming its high structure stability. Additionally, the presence of Ca is detected, attributed to the formation of insoluble Ca(OH)2 on the catalyst's surface during OER (Figure S45b), which may explain the observed performance decay in the alkaline seawater electrolysis.

Light-Assisted OER Performance and Mechanism. The light-assisted electrochemical OER performance of Fe-L-MoS₂ was further evaluated under UV–Vis irradiation in

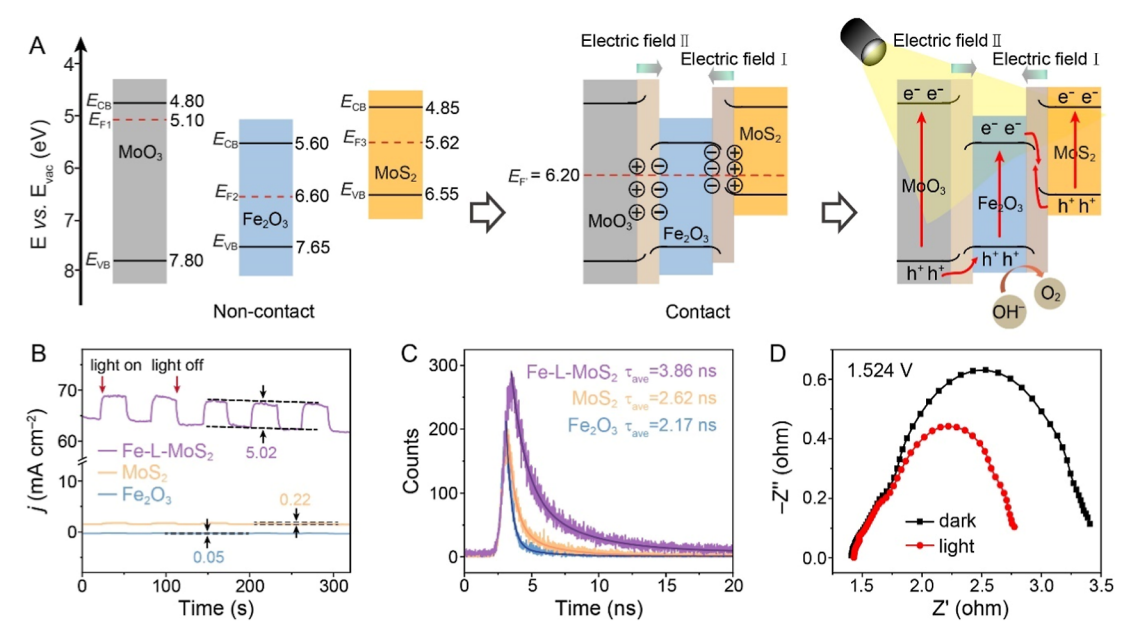


Figure 5. Mechanism of light-assisted OER. (A) Formation of built-in electric fields and migration routes of photogenerated carriers at the interfaces. E_{CB} and E_{VB} are conduction and valence band energies, respectively. (B) Transient photocurrent of Fe₂O₃, MoS₂, and Fe-L-MoS₂. (C) Time-resolved PL spectra of MoS₂, Fe₂O₃, and Fe-L-MoS₂. (D) Nyquist plots of Fe-L-MoS₂ in the dark and under light irradiation (at 1.524 V vs RHE).

alkaline seawater. At an applied potential of 1.550 V (vs RHE), the current density increases by 20.4% (Figure 4A), with a phototo-current efficiency (PCE) of 10.66%. The Tafel slope decreases from 48.9 to 41.9 mV dec⁻¹ under irradiation (Figure 4B), indicating accelerated OER kinetics. Compared to other light-responsive electrocatalysts, Fe-L-MoS2 exhibits superior light-assisted OER activity in 1 M KOH and seawater (Figure S46 and Table S6). Although designing electrolytic cells and catalysts for light-assisted water electrolysis poses challenges, this approach holds significant promise for seawater electrolysis by leveraging solar energy to reduce costs associated with long-distance power transmission, on-site power generation, and maintenance, making it a cost-effective solution in specific contexts. Encouraged by these promising results, a two-electrode electrolyzer was assembled using Fe-L-MoS₂ and 20% Pt/C as the anode and cathode, respectively, to evaluate light-assisted seawater splitting performance at large current densities. The Fe-L-MoS $_2$ llPt/C seawater electrolyzer delivers a current density of 0.5 A cm⁻² at a cell voltage of 2.476 V (Figure 4C), significantly lower than the benchmark RuO₂||Pt/C system (2.718 V). Moreover, during a 170 h chronopotentiometry test at 0.2 A cm⁻² (Figure 4D), the cell potential decreases under light irradiation and remains lower until the light is turned off, demonstrating stable light-assisted OER catalysis of Fe-L-MoS₂ in seawater. Postlight-assisted Ut test characterizations confirm the robustness of the $MoO_3/$ Fe₂O₃/MoS₂ heterojunction. XPS analysis reveals persistent MoO₄²⁻ and SO₄²⁻ anions (Figure S47), while TEM images show an intact crystalline/amorphous interface (Figure S48), indicating strong anticorrosion properties of the three-phase heterojunction.

To better understand the light-assisted OER mechanism, the band structures of MoS_2 , Fe_2O_3 , and MoO_3 before and after contact are illustrated in Figure 5A. The work functions (Φ) of MoS_2 , Fe_2O_3 , and $Fe\text{-L-MoS}_2$ were determined using ultraviolet photoelectron spectroscopy (UPS, Figure S49). The work function of MoS_2 (5.62 eV) is lower than that of Fe_2O_3

(6.60 eV), indicating that electrons spontaneously migrate from MoS₂ to Fe₂O₃ upon interface formation, thereby narrowing their Fermi level (E_F) gap. This electron transfer establishes a built-in electric field I, directed from MoS2 to Fe₂O₃, resulting in charge redistribution at the interface. Consequently, Fe₂O₃ becomes negatively charged while the surface of MoS₂ becomes electrophilic. The positively charged MoS₂ can attract electron-rich OH-, which is expected to enhance catalytic kinetics, while the negatively charged Fe₂O₃ improves corrosion resistance by repelling Cl-. A second builtin electric field II, directed from MoO₃ to Fe₂O₃, forms at the Fe₂O₃/MoO₃ interface. Under light irradiation, electrons are excited from valence band maximum (VBM) to conduction band minimum (CBM), leaving photogenerated holes in the VBM of those three components. The built-in electric fields drive the migration of these charge carriers across the interface. Specifically, electrons transfer from the CBM of Fe₂O₃ to MoS₂, recombining with photogenerated holes in the VBM of MoS₂ due to the influence of electric field I,⁶⁸ which generates holes with strong oxidation properties in the VBM of Fe₂O₃. Similarly, photogenerated holes in the VBM of MoO₃ migrate to Fe_2O_3 , while electrons in the CBM of Fe_2O_3 move to MoO_3 under the influence of electric field II. This results in the accumulation of photogenerated holes on Fe₂O₃, thereby promoting the water oxidation reaction.

To investigate the photoresponse behavior, transient photocurrent was measured at a constant potential of 1.524 V. The current density of Fe-L-MoS₂ increases immediately upon light exposure and returns to its initial level when the light is turned off, indicating a rapid photoresponse (Figure 5B). While MoS₂ and Fe₂O₃ also exhibit photoresponse, their photocurrents (0.22 and 0.05 mA cm⁻², respectively) are substantially lower than that of Fe-L-MoS₂ (5.02 mA cm⁻²), further suggesting enhanced utilization efficiency of photogenerated carriers in the hybrid. Additionally, photoluminescence (PL) emission spectroscopy was employed to assess the recombination of photogenerated electron—hole pairs. A higher intensity in the

PL spectrum typically indicates a greater recombination rate of photogenerated carriers.⁶⁹ All catalysts exhibit a broad band in the range between 480 and 600 nm, suggesting multiple radiation processes of excited carriers (Figure S50). Notably, Fe-L-MoS₂ displays lower emission intensity compared to MoS₂ and Fe₂O₃, indicating that the three-phase heterointerfaces effectively mitigate carrier recombination. Timeresolved PL spectroscopy was further utilized to investigate charge dynamics. The carrier lifetime of Fe-L-MoS₂ is determined to be 3.86 ns (Figure 5C and Table S7), which is 1.77 and 1.47 times longer compared to Fe₂O₃ (2.17 ns) and MoS₂ (2.62 ns), respectively. This longer carrier lifetime can be ascribed to efficient carrier separation and reduced recombination. Moreover, the charge transfer resistance between the catalyst and electrolyte is decreased from 2.0 to 1.43 Ω under light irradiation (Figure 5D), reducing charge loss. This reduction is likely due to photogenerated holes acting as electron traps, attracting OH- reactants.34 Consequently, the charge concentration of Fe-L-MoS₂ increases nearly 5-fold under light irradiation (Figure S51), consistent with EIS and transient photocurrent results, further confirming that light irradiation generates more carriers to participate in catalytic reactions.

CONCLUSIONS

This study demonstrates that the construction of photo- and electric-active MoO₃/Fe₂O₃/MoS₂ heterojunctions significantly enhances light-assisted seawater oxidation while simultaneously protecting Fe₂O₃ from chlorine-induced corrosion. The amorphous/crystalline interfaces in Fe-L-MoS₂, characterized by a nanoparticle-decorated structure, expand the ECSA and provide abundant active sites. These heterointerfaces facilitate the OER process and, along with in situ leached MoO₄²⁻ and SO₄²⁻, mitigate Cl⁻ adsorption, thereby suppressing electrode corrosion. Additionally, built-in electric fields promote charge migration and decrease the recombination of photogenerated carriers, leading to increased participation of photocarriers in the OER process. As a result, Fe-L-MoS₂ exhibits significantly enhanced OER activity and durability in alkaline seawater, achieving 10 mA cm⁻² at 267 mV with remarkable long-term stability, showing only a 2.2% activity loss over 500 h at 300 mA cm⁻². Light irradiation excites Fe-L-MoS₂, generating carriers and reducing interfacial resistance, resulting in a 20.4% increase in seawater oxidation current density. When combined with a Pt/C cathode, the Fe-L-MoS₂||Pt/C cell, assisted by light irradiation, requires only 2.476 V to reach 0.5 A cm⁻² in seawater, demonstrating stable operation for over 170 h at 0.2 A cm⁻². This study introduces a novel design concept for OER electrocatalysts that integrate excellent photoelectric synergistic effects with strong anticorrosion properties for scalable seawater electrolysis, offering a promising strategy for future energy applications.

ASSOCIATED CONTENT

Data Availability Statement

Data is available upon reasonable request to the corresponding author.

Supporting Information

The Supporting Information is available free of charge at https://pubs.acs.org/doi/10.1021/jacs.5c04085.

Chemicals, experimental methods, additional XRD, Raman, XPS, SEM, UPS, UV-vis spectrum, PL

spectrum, cyclic voltammogram, electrochemical performance, DFT simulation results, and crystal structure (PDF)

AUTHOR INFORMATION

Corresponding Authors

Byungchan Han – Department of Chemical and Biomolecular Engineering, Yonsei University, Seoul 03722, Republic of *Korea;* orcid.org/0000-0002-2325-6733; Email: bchan@yonsei.ac.kr

Lawrence Yoon Suk Lee - Department of Applied Biology and Chemical Technology and Research Institute for Smart Energy, The Hong Kong Polytechnic University, Kowloon, Hong Kong SAR, China; Department of Chemical Engineering (Integrated Engineering), Kyung Hee University, Yongin-si, Gyeonggi-do 17104, Republic of Korea; orcid.org/0000-0002-6119-4780;

Email: lawrence.ys.lee@polyu.edu.hk

Authors

Zhen Li – Department of Applied Biology and Chemical Technology and Research Institute for Smart Energy, The Hong Kong Polytechnic University, Kowloon, Hong Kong SAR, China

Wei Tao - Department of Chemical and Biomolecular Engineering, Yonsei University, Seoul 03722, Republic of

Ying Wang - Department of Applied Biology and Chemical Technology and Research Institute for Smart Energy, The Hong Kong Polytechnic University, Kowloon, Hong Kong SAR, China; orcid.org/0000-0003-3212-9653

Xucun Ye - Department of Applied Biology and Chemical Technology and Research Institute for Smart Energy, The Hong Kong Polytechnic University, Kowloon, Hong Kong SAR, China

Yiqun Chen - Department of Applied Biology and Chemical Technology and Research Institute for Smart Energy, The Hong Kong Polytechnic University, Kowloon, Hong Kong SAR, China

Complete contact information is available at: https://pubs.acs.org/10.1021/jacs.5c04085

Author Contributions

^{||}Z. L. and W. T. contributed equally to this work.

The authors declare no competing financial interest.

ACKNOWLEDGMENTS

The authors gratefully acknowledge the State Key Laboratory of Chemical Biology and Drug Discovery Center for PL measurements, the financial support from the Hong Kong Polytechnic University (Q-CDAG), and the National Research Foundation of Korea (NRF-2022H1D3A2A01096400) of the Korean Government (MSIT). Z.L. acknowledges the award of the PolyU Presidential PhD Fellowship Scheme.

REFERENCES

(1) Sanati, S.; Morsali, A.; Garcia, H. First-row transition metalbased materials derived from bimetallic metal-organic frameworks as highly efficient electrocatalysts for electrochemical water splitting. Energy Environ. Sci. 2022, 15, 3119-3151.

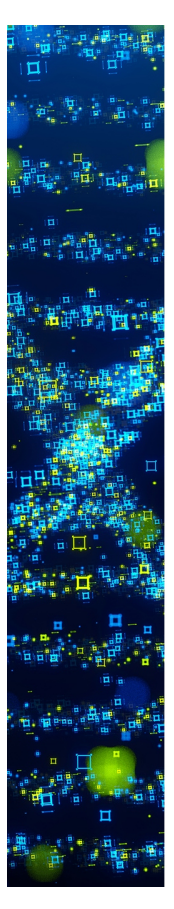
- (2) Zhu, J.; Hu, L. S.; Zhao, P. X.; Lee, L. Y. S.; Wong, K. Y. Recent advances in electrocatalytic hydrogen evolution using nanoparticles. *Chem. Rev.* **2020**, *120*, 851–918.
- (3) Guo, Y. N.; Park, T.; Yi, J. W.; Henzie, J.; Kim, J.; Wang, Z. L.; Jiang, B.; Bando, Y.; Sugahara, Y.; Tang, J.; et al. Nanoarchitectonics for transition-metal-sulfide-based electrocatalysts for water splitting. *Adv. Mater.* **2019**, *31*, 1807134.
- (4) Lu, F.; Zhou, M.; Zhou, Y. X.; Zeng, X. H. First-row transition metal based catalysts for the oxygen evolution reaction under alkaline conditions: Basic principles and recent advances. *Small* **2017**, *13*, 1701931.
- (5) Gao, L. K.; Cui, X.; Sewell, C. D.; Li, J.; Lin, Z. Q. Recent advances in activating surface reconstruction for the high-efficiency oxygen evolution reaction. *Chem. Soc. Rev.* **2021**, *50*, 8428–8469.
- (6) Tong, W. M.; Forster, M.; Dionigi, F.; Dresp, S.; Sadeghi Erami, R.; Strasser, P.; Cowan, A. J.; Farràs, P. Electrolysis of low-grade and saline surface water. *Nat. Energy* **2020**, *5*, 367–377.
- (7) Peng, J.; Dong, W.; Wang, Z.; Meng, Y.; Liu, W.; Song, P.; Liu, Z. Recent advances in 2D transition metal compounds for electrocatalytic full water splitting in neutral media. *Mater. Today Adv.* 2020, 8, 100081.
- (8) Farràs, P.; Strasser, P.; Cowan, A. J. Water electrolysis: Direct from the sea or not to be? *Joule* **2021**, *5*, 1921–1923.
- (9) Li, S.; Chen, B. B.; Wang, Y.; Ye, M. Y.; van Aken, P. A.; Cheng, C.; Thomas, A. Oxygen-evolving catalytic atoms on metal carbides. *Nat. Mater.* **2021**, *20*, 1240–1247.
- (10) Wu, Z. P.; Zhang, H. B.; Zuo, S. W.; Wang, Y.; Zhang, S. L.; Zhang, J.; Zang, S. Q.; Lou, X. W. Manipulating the local coordination and electronic structures for efficient electrocatalytic oxygen evolution. *Adv. Mater.* **2021**, *33*, 2103004.
- (11) Wang, N.; Ou, P. F.; Hung, S. F.; Huang, J. E.; Ozden, A.; Abed, J.; Grigioni, I.; Chen, C. R.; Miao, R. K.; Yan, Y.; et al. Strong-proton-adsorption Co-based electrocatalysts achieve active and stable neutral seawater splitting. *Adv. Mater.* **2023**, *35*, 2210057.
- (12) Zhuang, L. Ž.; Li, J. K.; Wang, K. Y.; Li, Z. H.; Zhu, M. H.; Xu, Z. Structural buffer engineering on metal oxide for long-term stable seawater splitting. *Adv. Funct. Mater.* **2022**, *32*, 2201127.
- (13) Liu, C. H.; Zhang, N. S.; Li, Y.; Fan, R. L.; Wang, W. J.; Feng, J. Y.; Liu, C.; Wang, J. U.; Hao, W. C.; Li, Z. S.; et al. Long-term durability of metastable β -Fe₂O₃ photoanodes in highly corrosive seawater. *Nat. Commun.* **2023**, *14*, 4266.
- (14) Hegner, F. S.; Garces-Pineda, F. A.; Gonzalez-Cobos, J.; Rodriguez-Garcia, B.; Torrens, M.; Palomares, E.; Lopez, N.; Galan-Mascaros, J. R. Understanding the catalytic selectivity of cobalt hexacyanoferrate toward oxygen evolution in seawater electrolysis. *ACS Catal.* **2021**, *11*, 13140–13148.
- (15) Luo, X.; Ji, P. X.; Wang, P. Y.; Tan, X.; Chen, L.; Mu, S. C. Spherical Ni₃S₂/Fe-NiP_x magic cube with ultrahigh water/seawater oxidation efficiency. *Adv. Sci.* **2022**, *9*, 2104846.
- (16) Chang, J. F.; Wang, G. Z.; Yang, Z. Z.; Li, B. Y.; Wang, Q.; Kuliiev, R.; Orlovskaya, N.; Gu, M.; Du, Y. G.; Wang, G. F.; et al. Dual-doping and synergism toward high-performance seawater electrolysis. *Adv. Mater.* **2021**, *33*, 2101425.
- (17) Yu, L.; Wu, L. B.; McElhenny, B.; Song, S. W.; Luo, D.; Zhang, F. H.; Yu, Y.; Chen, S.; Ren, Z. F. Ultrafast room-temperature synthesis of porous S-doped Ni/Fe (oxy)hydroxide electrodes for oxygen evolution catalysis in seawater splitting. *Energy Environ. Sci.* **2020**, *13*, 3439–3446.
- (18) Zhang, H.; He, X.; Dong, K.; Yao, Y. C.; Sun, S. J.; Zhang, M.; Yue, M.; Yang, C. X.; Zheng, D. D.; Liu, Q.; et al. Selenate promoted stability improvement of nickel selenide nanosheet array with an amorphous NiOOH layer for seawater oxidation. *Mater. Today Phys.* 2023, 38, 101249.
- (19) Ma, T. F.; Xu, W. W.; Li, B. R.; Chen, X.; Zhao, J. J.; Wan, S. S.; Jiang, K.; Zhang, S. X.; Wang, Z. F.; Tian, Z. Q.; et al. The critical role of additive sulfate for stable alkaline seawater oxidation on nickel-based electrodes. *Angew. Chem., Int. Ed.* **2021**, *60*, 22740–22744.
- (20) Kuang, Y.; Kenney, M. J.; Meng, Y. T.; Hung, W. H.; Liu, Y. J.; Huang, J. E.; Prasanna, R.; Li, P. S.; Li, Y. P.; Wang, L.; et al. Solar-

- driven, highly sustained splitting of seawater into hydrogen and oxygen fuels. *Proc. Natl. Acad. Sci. U.S.A.* **2019**, *116*, 6624–6629.
- (21) Khatun, S.; Shimizu, K.; Pal, S.; Nandi, S.; Watanabe, S.; Roy, P. Enthralling anodic protection by molybdate on high-entropy alloy-based electrocatalyst for sustainable seawater oxidation. *Small* **2024**, 20, 2402720.
- (22) Haq, T.; Arooj, M.; Tahir, A.; Haik, Y. SO_x functionalized NiOOH nanosheets embedded in Ni(OH)₂ microarray for high-efficiency seawater oxidation. *Small* **2024**, 20, 2305694.
- (23) Li, D.; Qin, Y. Y.; Liu, J.; Zhao, H. Y.; Sun, Z. J.; Chen, G. B.; Wu, D. Y.; Su, Y. Q.; Ding, S. J.; Xiao, C. H. Dense crystalline-amorphous interfacial sites for enhanced electrocatalytic oxygen evolution. *Adv. Funct. Mater.* **2022**, *32*, 2107056.
- (24) Zhang, X. Y.; Li, Y. X.; Wu, Z. J.; Sheng, H. B.; Hu, Y. B.; Li, C.; Li, H. Y.; Cao, L. X.; Dong, B. H. Crystalline/amorphous composite interface induced by NaBH₄ hydrolysis reaction: A new interfacial electrocatalyst for efficient oxygen evolution reaction. *Mater. Today Energy* **2022**, *26*, 100987.
- (25) Zhang, Y. P.; Gao, F.; Wang, D. Q.; Li, Z. L.; Wang, X. M.; Wang, C. Q.; Zhang, K. W.; Du, Y. K. Amorphous/crystalline heterostructure transition-metal-based catalysts for high-performance water splitting. *Coord. Chem. Rev.* **2023**, 475, 214916.
- (26) Maiti, K.; Kim, N. H.; Lee, J. H. Strongly stabilized integrated bimetallic oxide of Fe₂O₃-MoO₃ nano-crystal entrapped N-doped graphene as a superior oxygen reduction reaction electrocatalyst. *Chem. Eng. J.* **2021**, *410*, 128358.
- (27) Wang, B. W.; Chen, X. X.; He, Y. J.; Liu, Q.; Zhang, X. X.; Luo, Z. Y.; Kennedy, J. V.; Li, J. H.; Qian, D.; Liu, J. L.; et al. Fe₂O₃/P-doped CoMoO₄ electrocatalyst delivers efficient overall water splitting in alkaline media. *Appl. Catal. B Environ. Energy* **2024**, 346, 123741.
- (28) Ma, X. Z.; Zhang, M. Y.; Aza, F. H.; Gao, Q.; Xu, Z. K.; Li, L.; Wu, L. L.; Zhang, X. T.; Chen, Y. J. Photothermal-effect-promoted interfacial OH^- filling and the conversion of carrier type in $(Co_{1-x}Ni_x)_3C$ during water oxidation. *J. Mater. Chem. A* **2022**, *10*, 8258–8267.
- (29) Han, X. L.; Yu, Y. F.; Huang, Y.; Liu, D. L.; Zhang, B. Photogenerated carriers boost water splitting activity over transition-metal/semiconducting metal oxide bifunctional electrocatalysts. *ACS Catal.* **2017**, *7*, 6464–6470.
- (30) Xu, H.; Shang, H. Y.; Jin, L. J.; Chen, C. Y.; Wang, C.; Du, Y. K. Boosting electrocatalytic oxygen evolution over Prussian blue analog/transition metal dichalcogenide nanoboxes by photo-induced electron transfer. *J. Mater. Chem. A* **2019**, *7*, 26905–26910.
- (31) Yang, Y. M.; Ji, Y. J.; Li, G. Y.; Li, Y. Y.; Jia, B. H.; Yan, J. Q.; Ma, T. Y.; Liu, S. Z. $IrO_x@In_2O_3$ heterojunction from individually crystallized oxides for weak-light-promoted electrocatalytic water oxidation. *Angew. Chem., Int. Ed.* **2021**, *60*, 26790–26797.
- (32) Ai, L. H.; Li, N.; Chen, M.; Jiang, H. L.; Jiang, J. Photothermally boosted water splitting electrocatalysis by broadband solar harvesting nickel phosphide within a quasi-MOF. *J. Mater. Chem. A* **2021**, *9*, 16479–16488.
- (33) Zhang, D. X.; Liu, Y. H.; Li, L. H.; Li, D.; Jiang, T. Y.; Huang, H.; Jiang, D. L.; Kang, Z. H.; Mao, B. D. Cu_3FeS_4 quantum dots as a single-component photo-assisted electrocatalyst for efficient hydrogen evolution. *J. Mater. Chem. A* **2023**, *11*, 1927–1936.
- (34) Meng, H. Y.; Xi, W.; Ren, Z. Y.; Du, S. C.; Wu, J.; Zhao, L.; Liu, B. W.; Fu, H. G. Solar-boosted electrocatalytic oxygen evolution via catalytic site remodelling of CoCr layered double hydroxide. *Appl. Catal. B Environ. Energy* **2021**, 284, 119707.
- (35) Dong, Q. W.; Li, M. L.; Sun, M. S.; Si, F. Y.; Gao, Q. Z.; Cai, X.; Xu, Y. H.; Yuan, T.; Zhang, S. S.; Peng, F.; et al. Phase-controllable growth Ni_xP_y modified CdS@Ni₃S₂ electrodes for efficient electrocatalytic and enhanced photoassisted electrocatalytic overall water splitting. *Small Methods* **2021**, *5*, 2100878.
- (36) Li, H.; Wang, S. Y.; Wang, M. T.; Gao, Y. Y.; Tang, J. B.; Zhao, S. L.; Chi, H. B.; Zhang, P. F.; Qu, J. S.; Fan, F. T.; et al. Enhancement of plasmon-induced photoelectrocatalytic water oxidation over Au/TiO₂ with lithium intercalation. *Angew. Chem., Int. Ed.* **2022**, *61*, No. e202204272.

- (37) Wang, P. P.; Ding, C. M.; Deng, Y. T.; Chi, H. B.; Zheng, H. B.; Liu, L.; Li, H.; Wu, Y. K.; Liu, X.; Shi, J. Y.; et al. Simultaneous improvement in hole storage and interfacial catalysis over Ni-Fe oxyhydroxide-modified tantalum nitride photoanodes. *ACS Catal.* 2023, 13, 2647–2656.
- (38) Niu, Q. Y.; Gu, X. T.; Li, L.; Zhang, Y. N.; Zhao, G. H. 3D CQDs-{001}TiO₂/Ti photoelectrode with dominant {001} facets: Efficient visible-light-driven photoelectrocatalytic oxidation of organic pollutants and mechanism insight. *Appl. Catal. B Environ. Energy* **2020**, *261*, 118229.
- (39) Shi, Q. J.; Li, J.; Liu, Y. B.; Kong, K. J.; Li, A. Z.; Duan, H. H. Photoelectrocatalytic valorization of biomass-derived succinic acid into ethylene coupled with hydrogen production over an ultrathin BiO_x-covered TiO₂. ACS Catal. **2024**, *14*, 10728–10736.
- (40) Lee, T. H.; Hillman, S. A. J.; Gonzalez-Carrero, S.; Difilippo, A.; Durrant, J. R. Long-Lived charges in Y6:PM6 bulk-heterojunction photoanodes with a polymer overlayer improve photoelectrocatalytic performance. *Adv. Energy Mater.* **2023**, *13*, 2300400.
- (41) Li, H. J.; Jian, L. H.; Chen, Y.; Wang, G. W.; Lyu, J. H.; Dong, X. L.; Liu, X. H.; Ma, H. C. Fabricating Bi₂MoO₆@Co₃O₄ core-shell heterogeneous architectures with Z-scheme for superior photoelectrocatalytic water purification. *Chem. Eng. J.* **2022**, 427, 131716.
- (42) Wang, J. C.; Zhou, T. S.; Zhang, Y.; Li, L.; Zhou, C. H.; Bai, J.; Li, J. H.; Zhu, H.; Zhou, B. X. Type-II heterojunction CdIn₂S₄/BiVO₄ coupling with CQDs to improve PEC water splitting performance Synergistically. ACS Appl. Mater. Interfaces 2022, 14, 45392–45402.
- (43) Divya, N. G.; Bushiri, M. J. High index facet bounded α -Fe₂O₃ pseudocubic nanocrystals with enhanced electrochemical properties: Zn²⁺ ion assisted solvo-hydrothermal synthesis. *CrystEngComm* **2019**, 21, 1378–1388.
- (44) Carvalho, B. R.; Wang, Y. X.; Mignuzzi, S.; Roy, D.; Terrones, M.; Fantini, C.; Crespi, V. H.; Malard, L. M.; Pimenta, M. A. Intervalley scattering by acoustic phonons in two-dimensional MoS₂ revealed by double-resonance Raman spectroscopy. *Nat. Commun.* **2017**, *8*, 14670.
- (45) Sharma, L.; Botari, T.; Tiwary, C. S.; Halder, A. Hydrogen evolution at the in situ MoO₃/MoS₂ heterojunctions created by nonthermal O₂ plasma treatment. ACS Appl. Energy Mater. **2020**, *3*, 5333–5342.
- (46) Kalus, M. R.; Barsch, N.; Streubel, R.; Gokce, E.; Barcikowski, S.; Gokce, B. How persistent microbubbles shield nanoparticle productivity in laser synthesis of colloids quantification of their volume, dwell dynamics, and gas composition. *Phys. Chem. Chem. Phys.* **2017**, *19*, 7112–7123.
- (47) Shakeri, M. S.; Polit, O.; Grabowska-Polanowska, B.; Pyatenko, A.; Suchanek, K.; Dulski, M.; Gurgul, J.; Swiatkowska-Warkocka, Z. Solvent-particles interactions during composite particles formation by pulsed laser melting of α -Fe₂O₃. Sci. Rep. **2022**, 12, 11950.
- (48) Narengerile, T. W.; Watanabe, T. Acetone decomposition by water plasmas at atmospheric pressure. *Chem. Eng. Sci.* **2012**, *69*, 296–303.
- (49) Wang, J. C.; Ren, J.; Yao, H. C.; Zhang, L.; Wang, J. S.; Zang, S. Q.; Han, L. F.; Li, Z. J. Synergistic photocatalysis of Cr(VI) reduction and 4-Chlorophenol degradation over hydroxylated α -Fe₂O₃ under visible light irradiation. *J. Hazard. Mater.* **2016**, 311, 11–19.
- (50) Deng, J.; Ye, C.; Cai, A. H.; Huai, L. Y.; Zhou, S. Q.; Dong, F. L.; Li, X. Y.; Ma, X. Y. S-doping α -Fe₂O₃ induced efficient electronhole separation for enhanced persulfate activation toward carbamazepine oxidation: Experimental and DFT study. *Chem. Eng. J.* **2021**, 420, 129863.
- (51) Alrasheed, A.; Gorham, J. M.; Khac, B. C. T.; Alsaffar, F.; DelRio, F. W.; Chung, K. H.; Amer, M. R. Surface properties of laser-treated molybdenum disulfide nanosheets for optoelectronic applications. ACS Appl. Mater. Interfaces 2018, 10, 18104—18112.
- (52) Guo, L. Q.; Chen, F.; Fan, X. Q.; Cai, W. D.; Zhang, J. L. Sdoped α -Fe₂O₃ as a highly active heterogeneous Fenton-like catalyst towards the degradation of acid orange 7 and phenol. *Appl. Catal. B Environ. Energy* **2010**, *96*, 162–168.

- (53) Ran, J. R.; Guo, W. W.; Wang, H. L.; Zhu, B. C.; Yu, J. G.; Qiao, S. Z. Metal-free 2D/2D phosphorene/g-C₃N₄ Van der Waals heterojunction for highly enhanced visible-light photocatalytic H₂ production. *Adv. Mater.* **2018**, *30*, 1800128.
- (54) Chen, X. L.; Shi, T.; Zhong, K. L.; Wu, G. L.; Lu, Y. Capacitive behavior of MoS₂ decorated with FeS₂@carbon nanospheres. *Chem. Eng. J.* **2020**, 379, 122240.
- (55) Ye, J.; Zang, Y. P.; Wang, Q. Y.; Zhang, Y. D.; Sun, D.; Zhang, L. J.; Wang, G. M.; Zheng, X. S.; Zhu, J. F. Nitrogen doped FeS₂ nanoparticles for efficient and stable hydrogen evolution reaction. *J. Energy Chem.* **2021**, *56*, 283–289.
- (56) Liu, J. Y.; Liu, X.; Shi, H.; Luo, J. H.; Wang, L.; Liang, J. S.; Li, S. Z.; Yang, L. M.; Wang, T. Y.; Huang, Y. H.; et al. Breaking the scaling relations of oxygen evolution reaction on amorphous NiFeP nanostructures with enhanced activity for overall seawater splitting. *Appl. Catal. B Environ. Energy* **2022**, 302, 120862.
- (57) Song, H. J.; Yoon, H.; Ju, B.; Lee, D. Y.; Kim, D. W. Electrocatalytic selective oxygen evolution of carbon-coated $Na_2Co_{1-x}Fe_xP_2O_7$ nanoparticles for alkaline seawater electrolysis. *ACS Catal.* **2020**, *10*, 702–709.
- (58) Ye, P. C.; Fang, K. Q.; Wang, H. Y.; Wang, Y. H.; Huang, H.; Mo, C. B.; Ning, J. Q.; Hu, Y. Lattice oxygen activation and local electric field enhancement by co-doping Fe and F in CoO nanoneedle arrays for industrial electrocatalytic water oxidation. *Nat. Commun.* **2024**, *15*, 1012.
- (59) Guan, M. Q.; Wang, C.; Li, S.; Du, H. W.; Yuan, Y. P. Understanding the enhanced electrocatalytic hydrogen evolution via integrating electrochemically inactive g-C₃N₄: the effect of interfacial engineering. *ACS Sustain. Chem. Eng.* **2020**, *8*, 10313–10320.
- (60) Chen, M. X.; Zhang, Y. Y.; Wang, R.; Zhang, B.; Song, B.; Guan, Y. C.; Li, S. W.; Xu, P. Surface reconstruction of Se-doped NiS_2 enables high-efficiency oxygen evolution reaction. *J. Energy Chem.* **2023**, *84*, 173–180.
- (61) Ran, N. A.; Song, E. H.; Wang, Y. W.; Zhou, Y.; Liu, J. J. Dynamic coordination transformation of active sites in single-atom MoS₂ catalysts for boosted oxygen evolution catalysis. *Energy Environ. Sci.* **2022**, *15*, 2071–2083.
- (62) Yang, Z. H.; Wang, S.; Wei, C. Y.; Chen, L.; Xue, Z. M.; Mu, T. C. Proton transfer mediator for boosting the current density of biomass electrooxidation to the ampere level. *Energy Environ. Sci.* **2024**, *17*, 1603–1611.
- (63) Lu, Y. X.; Liu, T. Y.; Dong, C. L.; Huang, Y. C.; Li, Y. F.; Chen, J.; Zou, Y. Q.; Wang, S. Y. Tuning the selective adsorption site of biomass on Co₃O₄ by Ir single atoms for electrosynthesis. *Adv. Mater.* **2021**, 33, 2007056.
- (64) Jain, D.; Mamtani, K.; Gustin, V.; Gunduz, S.; Celik, G.; Waluyo, I.; Hunt, A.; Co, A. C.; Ozkan, U. S. Enhancement in oxygen reduction reaction activity of nitrogen-doped carbon nanostructures in acidic media through chloride-ion exposure. *Chemelectrochem* **2018**, *5*, 1966–1975.
- (65) Kang, X.; Yang, F. N.; Zhang, Z. Y.; Liu, H. M.; Ge, S. Y.; Hu, S. Q.; Li, S. H.; Luo, Y. T.; Yu, Q. M.; Liu, Z. B.; et al. A corrosion-resistant RuMoNi catalyst for efficient and long-lasting seawater oxidation and anion exchange membrane electrolyzer. *Nat. Commun.* 2023, 14, 3607.
- (66) Zhang, F. H.; Liu, Y. F.; Wu, L. B.; Ning, M. H.; Song, S. W.; Xiao, X.; Hadjiev, V. G.; Fan, D. E.; Wang, D. Z.; Yu, L.; et al. Efficient alkaline seawater oxidation by a three-dimensional core-shell dendritic NiCo@NiFe layered double hydroxide electrode. *Mater. Today Phys.* **2022**, *27*, 100841.
- (67) Li, Z.; Huang, F.; Xu, Y. F.; Yan, A. H.; Dong, H. M.; Xiong, X.; Zhao, X. H. Electron-extracting system with enhanced photocatalytic hydrogen production performance: synergistic utilization of Z-scheme and Ohmic heterojunctions. *Chem. Eng. J.* **2022**, 429, 132476.
- (68) Jiang, Z. F.; Wan, W. M.; Li, H. M.; Yuan, S. Q.; Zhao, H. J.; Wong, P. K. A hierarchical Z-scheme α -Fe₂O₃/g-C₃N₄ hybrid for enhanced photocatalytic CO₂ Reduction. *Adv. Mater.* **2018**, *30*, 1706108.

(69) Huang, F.; Li, Z.; Xu, Y. F.; Yan, A. H.; Zhang, T. Y.; Wang, Q. D.; Li, S. H.; Lu, S. J.; Zhao, W. X.; Gao, Y.; et al. Excellent anti-photocorrosion and hydrogen evolution activity of $ZnIn_2S_4$ -based photocatalysts: In-situ design of photogenerated charge dynamics. *Chem. Eng. J.* **2023**, 473, 145430.



CAS BIOFINDER DISCOVERY PLATFORM™

STOP DIGGING THROUGH DATA —START MAKING DISCOVERIES

CAS BioFinder helps you find the right biological insights in seconds

Start your search

